Inside a nanocrystal-based photodiode using photoemission microscopy

Mariarosa Cavallo, Rodolphe Alchaar, Erwan Bossavit, Huichen Zhang, Tung Huu Dang, Adrien Khalili, Yoann Prado, Mathieu Silly, James Utterback, Sandrine Ithurria, et al.

Inside a nanocrystal-based photodiode using photoemission microscopy

Mariarosa Cavallo[1], Rodolphe Alchaar[1], Erwan Bossavit[1,2], Huichen Zhang[1], Tung Huu Dang[1], Adrien Khalili[1], Yoann Prado[1], Mathieu G. Silly[2], James K. Utterback[1], Sandrine Ithurria[3], Pavel Dudin[2], José Avila[2], Debora Pierucci[1], Emmanuel Lhuillier[1]*

[1] Sorbonne Université, CNRS, Institut des NanoSciences de Paris, INSP, F-75005 Paris, France.
[2] Synchrotron SOLEIL, L'Orme des Merisiers, Départementale 128, 91190 Saint-Aubin, France.
[3] Laboratoire de Physique et d'Etude des Matériaux, ESPCI-Paris, PSL Research University, Sorbonne Université Univ Paris 06, CNRS UMR 8213, 10 rue Vauquelin 75005 Paris, France.

Abstract: As nanocrystal-based devices gain maturity, a comprehensive understanding of their electronic structure is necessary for further optimization. Most spectroscopic techniques typically examine pristine materials and disregard the coupling of the active material to its actual environment, the influence of an applied electric field, and possible illumination effects. Therefore, it is critical to develop tools that can probe device operation *in situ* and *operando*. Here we explore photoemission microscopy as a tool to unveil the energy landscape of a HgTe NC-based photodiode. We propose a planar diode stack to facilitate surface-sensitive photoemission measurements. We demonstrate that the method gives direct quantification of the diode's built-in voltage. Furthermore, we discuss how it is affected by particle size and illumination. We show that combining SnO_2 and Ag_2Te as electron and hole transport layers is better suited for extended-short-wave infrared materials than materials with larger bandgaps. We also identify the effect of photodoping over the SnO_2 layer and propose a strategy to overcome it. Given its simplicity, the method appears to be of utmost interest for screening diode design strategies.

Keywords: nanocrystals, HgTe, photoemission, electronic structure, photodiode, *pn* junction.

*To whom correspondence should be sent: el@insp.upmc.fr

INTRODUCTION

For a long time, infrared sensing has been dominated by epitaxially grown narrow-bandgap semiconductors (InGaAs, InSb, and HgCdTe) and heterostructures (type-II superlattice and GaAs/AlGaAs). These materials have undergone decades of optimization to achieve high quantum efficiencies;[1] however, despite this success, their high cost limits their use in defense and astronomy applications. This situation, therefore, calls for cost-effective alternative materials. Many materials have been explored, including 2D materials—such as graphene,[2] black phosphorus,[3,4] $Pt(Se/Te)_2$[5,6] and tellurene[7]—and colloidal nanocrystals[8] (NCs)—PbS,[9,10] PbSe,[11] HgTe,[12] HgSe,[13] Ag_2Se[14–16], etc. In this quest for alternatives, the primary challenge is to identify an infrared material that absorbs in the IR range and gives acceptable responsivity (the ability to convert light into an electrical signal). However, this is just the first step, as other requirements must be met before the commercialization of cameras that feature low noise, scalability (towards millions of pixels), and stability over time, temperature, and oxidation. Among the candidates, HgTe NCs[12] combine a broad spectral tunability and almost two decades of continuous research efforts[17,18] that have pushed the technology forward and brought demonstrations of high-performing photodiodes and cameras with a high-speed response.[19]

When it comes to the use of HgTe NCs in optoelectronic devices, multiple device geometries[20–22] (photoconductors, transistors, and diodes) and concepts, in particular the coupling to photonic cavities,[23] have been explored. At the single pixel level, performances have mostly been pushed in diode geometries for which detectivities close to those reported for commercial InGaAs have been achieved. Ackerman *et al.*[24] were the first to propose the coupling of an HgTe NC layer with an Ag_2Te layer, the latter being used as a hole extraction layer. Since then, many derivatives have been considered, in particular through the addition of an electron transport layer (Bi_2S_3,[25] CdSe,[26] SnO_2[27]), confirming the potential use of this specific diode stack for HgTe NC-based infrared sensing. To move beyond the already explored structures while avoiding an inefficient trial-and-error approach, deeper knowledge of the electronic structure must be correlated with the development of new diode stacks. Previous studies, either based on electrochemistry[28] or X-ray photoemission,[29] have already revealed the band alignment of HgTe NCs as a function of particle size and surface chemistry.[30] However, these previous studies focused on pristine samples, which completely neglects the electronic coupling existing in diodes as well as the impact of incident light. As a result, there is a need for new tools to probe *in situ* (*i.e.,* in a real diode) and *operando* (*i.e*., while the device is under operation) the electronic structure of NC-based photodiodes. Recently, X-ray photoemission microscopy[31–34] has been proposed as a tool that can combine imaging and photoemission spectroscopy. It consists of an X-ray nanobeam that is scanned on the surface of the sample, and for each point, we can acquire a kinetic energy photoemission spectrum. So far, this strategy has been mostly applied to 2D materials[32,35,36] by combining spatial information with angle-resolved photoemission to correlate spatial structure and electronic structure. Only very recently, Cavallo *et al.* proposed to use this strategy to probe the energy landscape of a NC-based field-effect transistor.[31] The method gives access to band bending and the electric field distribution under the application of drain and gate bias. Now, we aim to apply it to the case of a NC-based photodiode. However, the short escape depth of photoelectrons (a few nm) prevents the direct measurement of a diode stack by photoemission spectroscopy. We tackle this difficulty by designing a planar version of the diode stack and then probing the energy profile *in situ* and *operando* (here under illumination). In addition, we apply the method to unveil how the internal electric field is affected as the bandgap is changed.

METHODS

Chemicals: Mercury chloride ($HgCl_2$, Sigma-Aldrich, 99%), **Mercury compounds are highly toxic. Handle them with special care.** Tellurium powder (Te, Sigma-Aldrich, 99.99%), silver nitrate (Alfa Aesar, 99.9%), SnO_2 nanoparticles (15% dispersion in water, Alfa Aesar), trioctylphosphine (TOP, Alfa Aesar, 90%), oleylamine (OLA, Acros, 80-90%), dodecanethiol (DDT, Sigma-Aldrich, 98%), ammonium chloride (Alfa Aesar, 98 %) ethanol absolute (VWR), methanol (VWR, >98%), isopropanol (IPA, VWR), hexane (VWR, 99%), octane (Carlo erba, 99%), 2-mercaptoethanol (MPOH, Merck, >99%), N,N dimethylformamide (DMF, VWR), N-methylformamide (NMF, Alfa Aesar, 99%), toluene (VWR, 99.8%). All chemicals are used without further purification except oleylamine that is centrifuged before use.

1 M TOP:Te precursor: In a three-neck flask, we mixed Tellurium powder (2.54 g) in 20 mL of trioctylphosphine. The flask is degassed under sub-mbar pressure at room temperature for 5 min and then the temperature is increased to 100 °C. The degassing of the flask is conducted for 20 additional minutes. The atmosphere is switched to nitrogen and the temperature is raised to 275 °C. The solution turns to a clear orange coloration. The heating mantle is removed and the temperature of the flask cools down. Its color changes to yellow. Finally, this solution of TOP:Te is used as stock solution and stored into a glove box for storage.

HgTe NC synthesis with band-edge at 6000 cm^{-1}: In a 50 mL three-neck flask, we have mixed 540 mg of $HgCl_2$ salt together with 50 mL of oleylamine. The flask is then degassed under reduced pressure at 110 °C. The solution is yellow and clear. Then, 2 mL of TOP:Te (1 M) are extracted from the glove box and are mixed with 8 mL of oleylamine. The atmosphere is replaced by nitrogen and the temperature tuned to 57 °C. The pre-heated TOP:Te solution is injected in the three neck flask and the solution turns dark after 1 min. After 3 min, we inject 10 mL of a mixture of 10% DDT in toluene and a water bath is used to prompt the drop of temperature. The content of the flask is split in 4 tubes and MeOH is added. After centrifugation, the pellets are redispersed using 10 mL of toluene in a single centrifuge tube. The solution is precipitated again using absolute EtOH. The formed pellet is redispersed in 8 mL of toluene. At this step, the NCs are centrifuged in fresh toluene to remove the lamellar phase. The solid phase is discarded by centrifugation and the supernatant filtered through a 0.22 µm PTFE filter.

HgTe NC synthesis with band-edge at 4000 cm^{-1}: In a 100 mL three-neck flask, 543 mg of $HgCl_2$ and 60 mL of oleylamine (OLA) are degassed from room temperature to 110 °C for an hour. The atmosphere is then switched to nitrogen and the solution is cooled down to 82 °C. A solution of 2 mL of TOP:Te (1 M) and 8 mL of OLA is quickly added to the flask. After 3 minutes, the reaction is quickly quenched by adding a mixture of 1 mL of DDT and 9 mL of toluene. The nanocrystals are precipitated with methanol and redispersed in toluene. Then the nanocrystals are precipitated with ethanol and redispersed in toluene. The solution is centrifugated as is. The pellet is eliminated and the supernatant is washed one more time. Finally, the HgTe NCs solution in toluene is filtered through a 0.22 µm PTFE filter. The obtained solution is used for further characterization and device fabrication.

Ag_2Te NC synthesis: In a 50 mL three neck flask, 170 mg of $AgNO_3$ are mixed together with 25 mL of oleylamine and 2.5 mL of oleic acid. The flask is then degassed under vacuum at room temperature for 15 min and then at 70 °C for 10 min. The atmosphere is replaced to nitrogen and 2.5 mL of TOP are added into the solution. Then, the temperature of the flask is raised to 160 °C. After 30 min, the solution becomes orange. At this step, 0.5 mL of TOP:Te (1M) is injected and the

reaction is quenched after 10 min with a water bath. The crude solution was stored in a freezer at –-20 °C. When needed, 800 µL of the unfrozen crude solution are precipitated with MeOH. After centrifugation the formed pellet is redispersed in a mixture containing 200 µL DDT and 600 µL of chlorobenzene. Then, the NCs are precipitated by addition of methanol. After centrifugation the pellet is dispersed using 800 µL of chlorobenzene. Again, the NCs are precipitated by addition of MeOH and centrifugation. The pellet is this time dispersed in 1.6 mL of a (9:1 volume ratio) mixture of hexane:octane.

SnO_2 NCs: The procedure is inspired from ref [37]. For lightly doped SnO_2 (SnO_2-L), we dilute 200 µL of commercial solution with 1 mL of 24 mM NH_4Cl solution in water. For heavily doped SnO_2 (SnO_2-H), we dilute 200 µL of commercial solution with 1 mL of 48 mM NH_4Cl solution in water.

Infrared spectroscopy: We use a Thermo-Fischer iS50 in attenuated total reflection (ATR) mode for absorption. The spectra are averaged over 32 scans and acquired with a 4 cm^{-1} resolution. To measure photocurrent spectrum, a Femto DLPCA 200 current amplifier, is used to bias and magnify the output current from the sample. The output signal is then fed into the FTIR electronics. For PL, a film of NCs is excited using a blue flash light. This signal is then used as source for the FTIR.

Transmission electron microscopy on NCs: A dilute NC solution is drop-cast onto a copper grid covered with an amorphous carbon film. This grid is degassed under secondary vacuum to reduce future contamination. A JEOL 2010F microscope, operated at 200 kV, is used for acquisition of pictures.

Scanning electron microscopy and EDX mapping: SEM observations were carried out using a Zeiss Supra 40 microscope equipped with a Bruker XFlash 630M probe for energy dispersive X-ray (EDX) mapping. SEM images and EDX mapping were acquired at a voltage of 10 kV and an aperture of 10 µm. The EDX mapping duration was 1 hour.

Planar p-n junction fabrication: We start by cleaning the substrates with acetone and isopropyl alcohol and then placing them in an oxygen plasma cleaner for 10 minutes. The heavily doped SnO_2 solution is deposited onto the substrate via spin coating at 4000 rpm for 30 s. The film is annealed on a hot plate at 70°C for 1 h. Next, we created an interdigitated pattern with Ag_2Te using UV lithography. AZ5214E resist was spin-coated on the substrate at 4000 rpm for 30 s and then baked for 1.5 min at 110°C. The resist was then UV-exposed for 1.5 s in order to create the interdigitated pattern, followed by an inversion baking step for 2 min at 125°C and a second UV exposure for 40 s, without a mask. The resist was then developed using AZ726 for 30 s. Ag_2Te was spin-coated on top of the resist at 1500 rpm for 30 s, followed by an acetone lift-off to reveal the pattern. The final step in the process is the deposition of the HgTe ink solution. Ink preparation starts by dissolving 30 mg of $HgCl_2$ in a solution of 18 mL of DMF and 2 mL of mercaptoethanol. At each step, the solution is stirred with a vortex and an ultrasonic bath. HgTe nanocrystal solution (600 µL) is mixed with 600 µL of the exchange solution and 400 µL of DMF. Toluene is added to reach a global volume of 4 mL and the solution is centrifugated for 3 min at 6000 rpm to precipitate the nanoparticles. The supernatant is discarded, and the formed pellet is dried under vacuum for 3 mins and then redispersed in 500 µL of DMF to target a thickness of about 40 nm. The resulting ink is filtered and spin-coated on the substrate at 2000 rpm for 2 min followed by a drying step at 2500 rpm for 1 min.

Photoemission microscopy: The spatially resolved photoemission maps were measured at the ANTARES beamline of Synchrotron SOLEIL. We used linearly horizontal polarized photons with a photon energy of 95 eV and MBS A-1 hemispherical electron analyzer.[38] All measurements were conducted at 250 K, with an energy resolution better than 30 meV and a spatial resolution as low

as 500 nm along the pn junction (indicated as X-direction in all figures). For all maps, angular dispersion of the analyzer (±15°) is neglected by integrating the spectra over all angles. The samples were mounted on the *operando* sample holder of ANTARES beamline and directly grounded to it via silver paste. The sample holder was then grounded through the manipulator. The acquired data were processed using Wavemetrics Igor Pro. In particular, the binding energy maps were obtained by fitting a double gaussian to the measured spectra point-by-point and then plotting the binding energy value of the Hg $5d_{5/2}$ contribution. To evaluate the energy shift, the photoemission spectra were averaged over a small number of points (5 or 10) in the regions of interest. Binding energy calibration was performed by measuring the Fermi edge of a gold substrate mounted on the same sample holder of the device.

High-resolution photoemission spectroscopy: To characterize the pristine HgTe materials, additional non-spatially resolved measurements were performed at Tempo beamline[39] of synchrotron Soleil. Films of NCs were spin-cast onto a Si substrate coated with 80 nm of gold. The ligands of the NCs were exchanged using the same procedure as for device fabrication to avoid any charging effects during measurements. The samples were introduced in the preparation chamber and degassed under a vacuum below 10^{-9} mbar for at least two hours. Then the samples were introduced into the analysis chamber. The signal was acquired with an MBS A-1 photoelectron analyzer. The acquisition was done at a constant pass energy (50 eV) within the detector. A photon energy of 150 eV was used for the acquisition of valence band and work function while a 600 eV photon energy was used for the analysis of the core levels. A gold substrate was used to calibrate the Fermi energy. The absolute value of the incoming photon energy was determined by measuring the second order of Au 4f core level peaks. Then for a given analyzer pass energy, we measured the Fermi edge and set its binding energy as zero. The same shift was applied to all spectra acquired with the same pass energy. To determine the work function, we applied 18 V bias, whose exact value was determined by looking at the shift of a Fermi edge.

RESULTS AND DISCUSSION

We start by growing HgTe NCs that are relevant for short-wave infrared (SWIR) detection. We use the procedure developed by Keuleyan *et al.*,[40] in which $HgCl_2$ is reacted with telluride complexed to trioctylphosphine. The reaction is conducted at a mild temperature (≈60°C). The obtained particles have a branched aspect according to transmission electron microscopy, see **Figure 1**b. The reaction duration is appropriately selected to achieve a band edge at around 1.7 µm by the end of the NC growth, see **Figure 1**a. Initially, the particles are capped with long ligands (dodecanethiol) that are replaced by shorter ligands[41,42] (mercaptoethanol and $HgCl_2$) to increase the coupling and render the film photoconductive. By doing so, the absorption spectrum is redshifted, and the cut-off wavelength becomes 2 µm, as shown in **Figure 1**e.

For SWIR detection, Gréboval *et al.*[27] have proposed the use of a diode stack in which the HgTe NCs are sandwiched between SnO_2 and Ag_2Te, respectively, as electron and hole transport layers, see **Figure 1**d. Such a diode stack has demonstrated high performances at room temperature, with a responsivity of 300 $mA.W^{-1}$ under 0 V operation, detectivity of $5x10^{10}$ Jones, and a fast time response.

The particles have been further characterized using high-resolution X-ray photoemission. To ensure accurate representation of the material in the device and prevent possible charging-induced electrostatic shifts, similar surface chemistry processing was carried out. Beyond the Hg and Te states, the film presents contributions of C and Cl that come from the ligands (respectively, the mercaptoethanol and $HgCl_2$ used as a Hg source), see **Figure 1**c. On the other hand, we observe

no contribution coming from oxygen (O 1s state is expected to appear with a 532 eV binding energy) despite the preparation of the sample in air, which confirms the weak oxidation susceptibility of HgTe.[43]

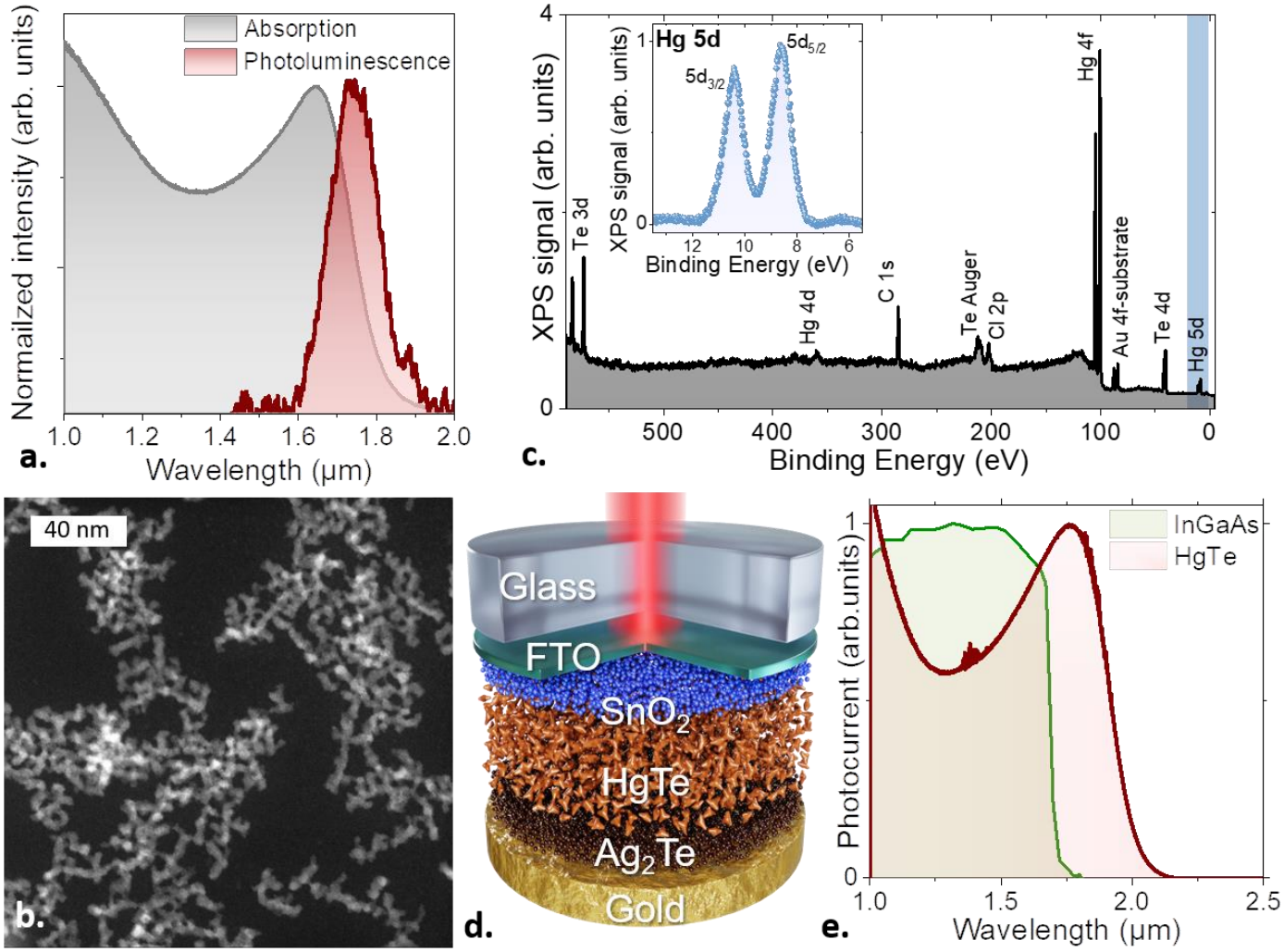

Figure 1 HgTe as active material for infrared photodiodes*. a. Absorption and photoluminescence spectra of HgTe NCs with a 1.6 μm band edge after synthesis. b. TEM image of the same HgTe NCs. c. Photoemission survey spectra for the same HgTe NCs, acquired with a photon energy of 700 eV. The inset is a zoom-in on the Hg 5d core level state, which has a low (8.2 eV) binding energy. d. Schematic representation of a short wave infrared photodiode with the infrared absorbing layer made of HgTe NCs. e. Photocurrent spectra for the diode depicted in part d. Note that in the diode, the cut-off wavelength now reaches 2 μm. The room temperature spectrum of an InGaAs photodiode is also depicted.*

The photoemission spectrum also presents a low binding energy peak of Hg 5d at 8.2 eV, see the inset of **Figure 1**c. Such low-binding energy states are crucial since they are required to perform soft X-ray photoemission microscopy. In these experiments, a Fresnel zone plate is used to focus the X-ray beam, here obtained from a synchrotron beam, see **Figure 2**b. The initial beam with a 50 μm width is focused to obtain a width of around 700 nm on the sample.[33] However, this zone plate is optimized for low-energy photons (<100 eV), requiring the presence of low-energy binding states in the sample to be spatially tracked. The use of low-energy photons also reduces the escape depth of the generated photoelectrons to a distance of less than 1 nm which is significantly lower than that of a conventional diode stack that is ≈500 nm thick. As a result, this technique is not suited to probe a diode with a conventional vertical geometry. Consequently, we have updated the device's geometry to be compatible with photoemission microscopy requiring that the probed surface be on top. We fabricated a planar version of the stack depicted in **Figure 1**d. The planar p-n junction

(**Figure 2**a) is built on a gold-coated Si wafer in which the gold layer forms an equipotential that minimizes sample charging. An SnO_2 layer is deposited on top of gold and then functionalized with an interdigitated electrode geometry using conventional optical lithography. Ag_2Te NCs are spin-coated in the opening of the resist. After liftoff, the Ag_2Te pattern on SnO_2 is covered by a HgTe NC film. Figure S1 depicts the fabrication procedure for the planar *p-n* junction, and Figure S2 shows its chemical mapping.

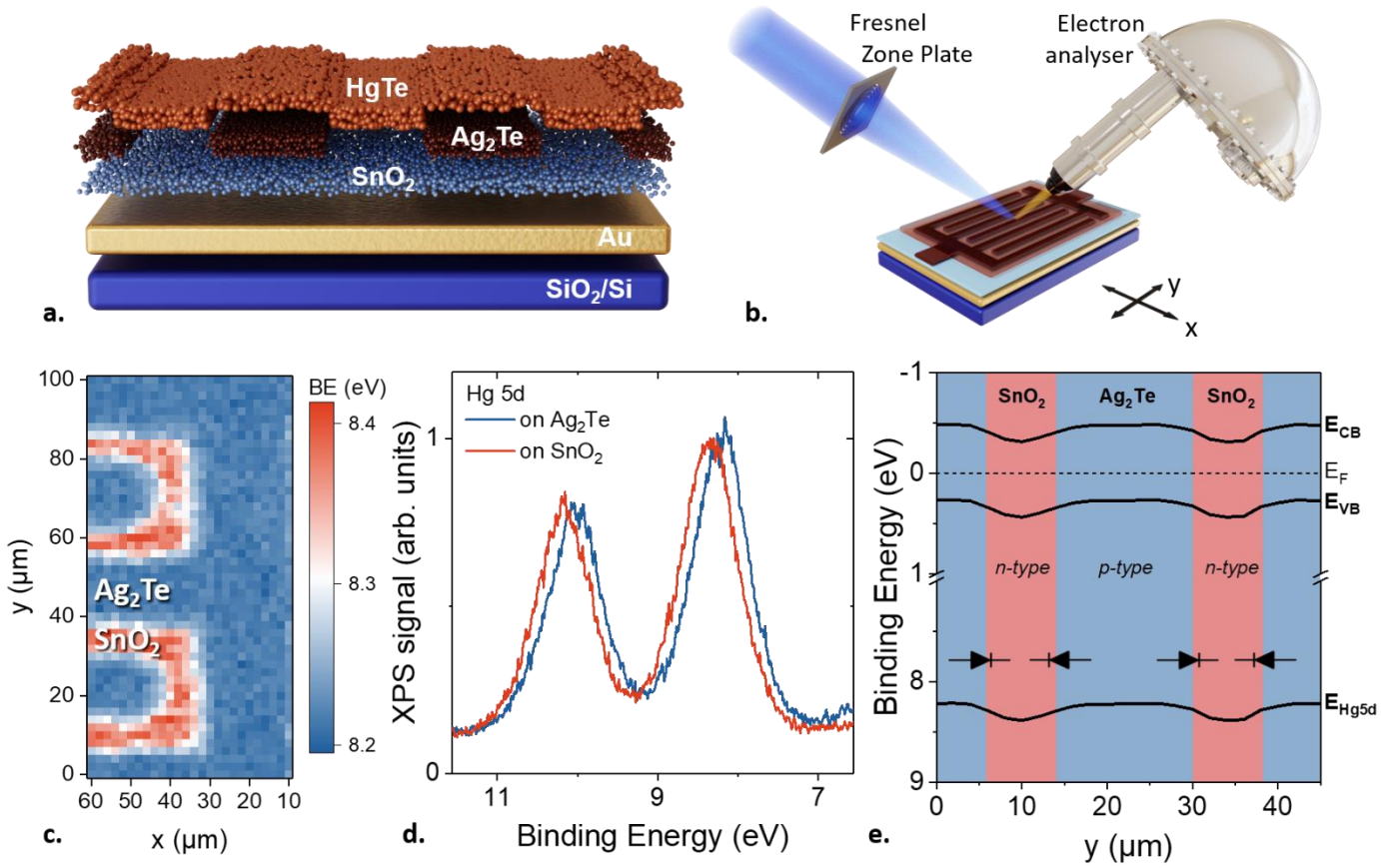

Figure 2. X-ray photoemission microscopy applied to a planar p-n junction. *a. Schematic representation of a planar p-n junction with the active layer made of HgTe NCs and where the n and p type characters are induced by the underlying charge transport layer (Ag_2Te for p side and SnO_2 for the n side). b. Conceptual representation of the photoemission microscopy. The soft X-ray beam from synchrotron is focused on the sample using a Fresnel zone plate. The sample is then scanned, and photoemitted electrons are analyzed using an electron analyzer. c. Binding energy map of the Hg $5d_{5/2}$ state as the planar p-n junction is scanned around the edge of the digit. d. Photoemission spectra of the Hg5d state acquired on top of the Ag_2Te area and on top of the SnO_2 area. e. Reconstructed valence and conduction band landscape of the planar heterojunction, assuming a rigid shift of the bands.*

Figure 2c shows a map of the binding energy of the Hg $5d_{5/2}$ state around the edge of two interdigitated fingers, obtained by fitting each acquired spectrum with a gaussian line shape. The contrast in the map reflects the underlying sample structure resulting from a shift in binding energy, as shown in **Figure 2**d.

Due to the strong interaction of electrons with matter, the photoelectron escape depth is short (few nm at the used photon energy), thus photoemission probes only the top surface of the sample. It remains that this surface experiences the influence of the textured substrate that is underneath, in what we can call a “remote doping”. This situation is nevertheless representative of what occurs in

a vertical stack (**Figure 1**d): as the absorbing layer is few hundred nm thick, HgTe being almost an intrinsic semiconductor (Figure S3), the p-n junction that is formed is the result of the behavior induced by the electron and hole transport layers at each side of this layer.

The Hg 5d state from HgTe NCs in contact with the SnO_2 layer presents, on average, a 140 meV shift towards higher binding energy, making the material more n-type. Assuming a rigid shift between the core level and the valence band, see **Figure 2**e, we can reconstruct the valence and conduction band diagram across two digits of the structure. The complete procedure is detailed in Figure S3. The observed shift induced by the substrate, of a magnitude comparable to the material's bandgap (≈0.5 eV), is large enough to induce a shift from *n*-type over SnO_2 to *p*-type over Ag_2Te, see **Figure 2**e. Consequently, photoemission microscopy offers a clear benefit by allowing for a direct measurement of the built-in voltage that is generally only obtained through a modeling of the electrical measurements. Furthermore, we observe that the width of the space-charge region between the n- and p-sides of the junction (see area between purple dashed lines in **Figure 3**) is on the order of a few microns. This is wider than the resolution of the X-ray beam and wider than the thickness of a typical vertical diode stack (≈ 500 nm), suggesting that the entire HgTe layer in the diode stack is affected. As a result, in a vertical heterojunction, the charge transport layers on each side affect the whole HgTe layer, which can be used as an absorbing intrinsic layer. There is consequently no need to further dope the HgTe layer to design *p* and *n* zones, which was a challenge up to recently[44].

Then, we investigated the effect of HgTe NC size on the formation of the p-n junction energy profile. In particular, we tested slightly larger NCs with a band edge at 2.5 µm—a material relevant for extended short-wave infrared (e-SWIR) detection. In **Figure 3**, we make a comparison of the energy landscape for SWIR (2 µm cut off) and e-SWIR (2.5 µm cut off) over the same interdigitated pattern. The results show that the size of the area associated with low binding energy, occurring over Ag_2Te and associated with an induced p-type behavior, is much larger for the SWIR material than for the e-SWIR material. This behavior can be explained by the large difference between the effective masses of the electron and hole in HgTe. The heavy-hole band is barely dispersive and is associated with a mass 25 times[45] larger than that of the strongly dispersive light-hole band acting as the conduction band. As a result of this asymmetry and the lack of bulk bandgap, the confinement in HgTe is mostly occurring within the conduction band. As we switch from the SWIR to an e-SWIR material, the optical band gap reduces by 250 meV, which mostly translates into a shift of the conduction band energy, with the valence band being only marginally affected. This intuition has been further confirmed by a systematic measurement of the band alignment for HgTe versus size, as shown in Figure S4. Consequently, as the optical band gap is reduced, the Fermi level also gets much closer to the conduction band. This means that for the same surface chemistry (i.e., same dipole), the e-SWIR material will acquire a n-type character compared to the SWIR material. This trend is fully in line with what we observed in **Figure 3**, where the high binding energy (i.e., n-type) domains are larger for the e-SWIR material due to its pre-existing *n*-type nature.

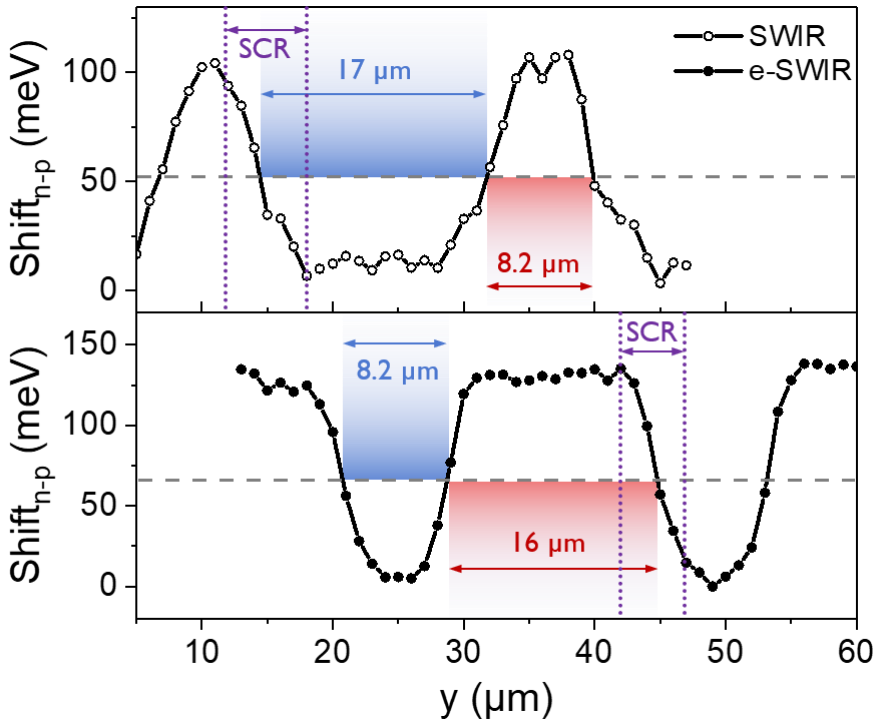

Figure 3 Effect of particle size on domain size. *Shift of the Hg 5d state across the planar p-n junction. Here two HgTe NCs have been used. Described as SWIR (top graph) is the material depicted in Figure 1 (with 2 µm cut-off wavelength), while the material described as e-SWIR (bottom graph) corresponds to larger HgTe particles (with 2.5 µm cut-off wavelength). The grey dashed line corresponds to half of the shift. Areas in pink are n-doped (from SnO_2), while areas in light blue are p-doped (from Ag_2Te). Purple dotted lines highlight the area corresponding to the space charge region (SCR).*

In the last part of this work, we explore *operando* conditions to closely mimic the realistic operation of the device and investigate the effect of incident light on its electronic structure. By doing so, multiple effects may be unveiled such as light induced damage, heating or photodoping. The sample located inside the microscope chamber is illuminated by a 635 nm laser diode. Mapping of the Hg5d state in the dark (resp. under illumination) is shown in **Figure 4**a (resp. **Figure 4**b). We observe a loss of contrast, which is more distinctly highlighted by the photoemission spectra. In the dark (**Figure 4**c), the shift between the peak over SnO_2 and over Ag_2Te is higher than the one observed under illumination (**Figure 4**d). The average values for these shifts are shown in **Figure 4**e. This suggests that the built-in electric field of the diode is reduced by a factor of 2 under illumination. However, it appears that the effect is not the same over the two parts of the diode. Indeed, the binding energy of the Hg 5d state from HgTe on top of Ag_2Te remains almost unchanged under illumination, see top part of **Figure 4**f, while the one from HgTe on top of SnO_2 is affected by the light, see the bottom part of **Figure 4**f.

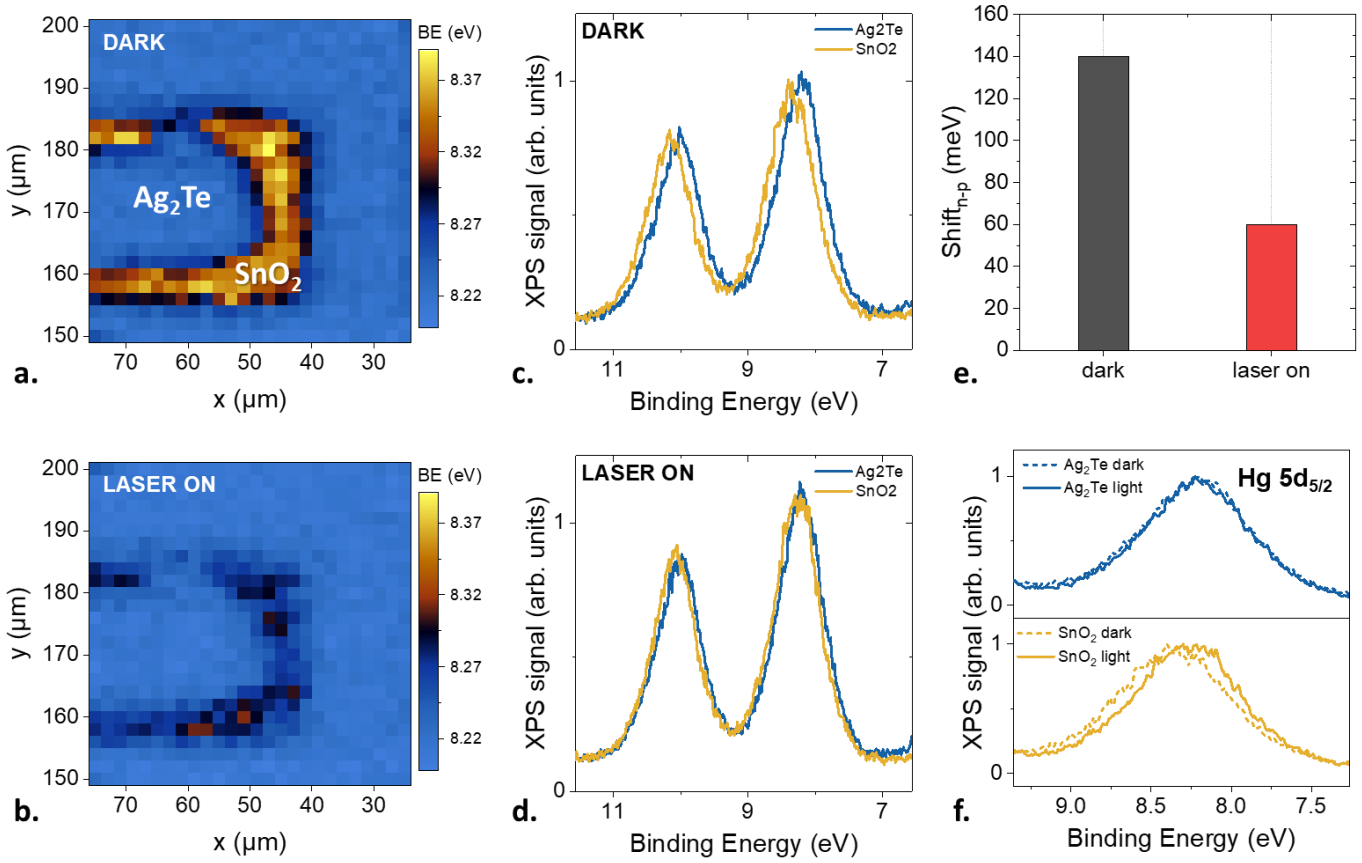

Figure 4* Operando *investigation of light on the electronic structure. *a. (resp b) Binding energy of the Hg $5d_{5/2}$ state across a planar p-n junction in the dark (resp under illumination by a laser diode at 635 nm). c. (resp d.) Photoemission spectra of the Hg5d state acquired on top of the Ag_2Te area and on top of the SnO_2 area in the dark (resp. under illumination by a laser diode at 635 nm). e. Average shift of the Hg 5d state binding energy across the junction in the dark and under illumination. f. Hg 5d core level spectra over Ag_2Te (top part) and over SnO_2 (bottom part) in the dark and under illumination.*

In oxides such as ZnO[46] or SnO_2, photodoping effects (i.e. accumulation of charge, often electron in oxide, in deep trap states resulting from unperfect passivation) are well known, and charge accumulation may build up under illumination acting against the designed built-in electric field. A possible strategy to overcome this undesired effect of light will be to push the extrinsic doping of the SnO_2 further to make it less sensitive to photocharge generation.

CONCLUSION

We used X-ray photoemission microscopy to probe the energy landscape of a nanocrystal-based photodiode under *in situ* and *operando* conditions. To meet the photoemission constraint, we proposed an updated planarized version of the device. The method gives a direct measurement of the built-in voltage of the diode, whereas most conventional methods only access this quantity through modeling of electrical measurements, making the method highly valuable for future device optimization. Moreover, this technique is compatible with measurements under illumination. Here we evidence a slight photodoping effect over the SnO_2 layer that counterbalances part of the diode electric field. The latter can likely be fixed by targeting higher doping of this layer. This work demonstrates that spatially resolved photoemission spectroscopy can be a highly valuable tool for optimizing optoelectronic devices based on nanocrystals.

SUPPORTING INFORMATION

Supporting Information include details about planar p-n junction fabrication and its chemical mapping, as well as band alignment for HgTe NCs with various sizes.

Author contributions

DP and EL designed the experiment and raised funding. YP and AK grew the particles with supervision of SI and EL. RA built the planar junction. All authors took part in the beamtime dedicated to photoemission microscopy or high-resolution photoemission. MC and JA conducted the data processing with support of DP. EL wrote the manuscript with input of all authors. All authors have proofread the final text.

ACKNOWLEDEGMENTS

The project is supported by ERC grant blackQD (grant n° 756225) and AQDtive (grant n°101086358). We acknowledge the use of clean-room facilities from the “Centrale de Proximité Paris-Centre”. This work has been supported by the Region Ile-de-France in the framework of DIM Nano-K (grant dopQD). This work was supported by French state funds managed by the ANR within the Investissements d'Avenir programme under reference ANR-11-IDEX-0004-02, and more specifically within the framework of the Cluster of Excellence MATISSE and also by the grant IPER-Nano2 (ANR-18CE30-0023-01), Copin (ANR-19-CE24-0022), Frontal (ANR-19-CE09-0017), Graskop (ANR-19-CE09-0026), NITQuantum (ANR-20-ASTR-0008), Bright (ANR-21-CE24-0012), MixDFerro (ANR-21-CE09-0029.), Quicktera (ANR-22-CE09-0018) and Operatwist (ANR-22-CE09-0037-01). This project has received financial support from the CNRS through the MITI interdisciplinary programs (project within).

CONFLICT OF INTEREST

The authors declare no competing interest.

REFERENCES

1 M. Kopytko and A. Rogalski, *Sens. Actuators Phys.*, 2022, **339**, 113511.
2 F. H. L. Koppens, T. Mueller, P. Avouris, A. C. Ferrari, M. S. Vitiello and M. Polini, *Nat. Nanotechnol.*, 2014, **9**, 780–793.
3 X. Chen, X. Lu, B. Deng, O. Sinai, Y. Shao, C. Li, S. Yuan, V. Tran, K. Watanabe, T. Taniguchi, D. Naveh, L. Yang and F. Xia, *Nat. Commun.*, 2017, **8**, 1672.
4 M. Engel, M. Steiner and P. Avouris, *Nano Lett.*, 2014, **14**, 6414–6417.
5 N. S. Azar, V. R. Shrestha, J. Bullock, M. Amani, H. Kim, A. Javey and K. B. Crozier, in *14th Pacific Rim Conference on Lasers and Electro-Optics (CLEO PR 2020) (2020), paper C11E_5*, Optica Publishing Group, 2020, p. C11E_5.
6 M. S. Shawkat, S. B. Hafiz, M. M. Islam, S. A. Mofid, M. M. Al Mahfuz, A. Biswas, H.-S. Chung, E. Okogbue, T.-J. Ko and D. Chanda, *ACS Appl. Mater. Interfaces*, 2021, **13**, 15542–15550.
7 C. Tan, M. Amani, C. Zhao, M. Hettick, X. Song, D.-H. Lien, H. Li, M. Yeh, V. R. Shrestha, K. B. Crozier, M. C. Scott and A. Javey, *Adv. Mater.*, 2020, **32**, 2001329.
8 T. Nakotte, S. G. Munyan, J. W. Murphy, S. A. Hawks, S. Kang, J. Han and A. M. Hiszpanski, *J. Mater. Chem. C*, 2022, **10**, 790–804.
9 J. S. Steckel, E. Josse, A. G. Pattantyus-Abraham, M. Bidaud, B. Mortini, H. Bilgen, O. Arnaud, S. Allegret-Maret, F. Saguin, L. Mazet, S. Lhostis, T. Berger, K. Haxaire, L. L. Chapelon, L. Parmigiani, P. Gouraud, M. Brihoum, P. Bar, M. Guillermet, S. Favreau, R. Duru, J. Fantuz, S. Ricq, D. Ney, I. Hammad, D. Roy, A. Arnaud, B. Vianne, G. Nayak, N. Virollet, V. Farys, P.

Malinge, A. Tournier, F. Lalanne, A. Crocherie, J. Galvier, S. Rabary, O. Noblanc, H. Wehbe-Alause, S. Acharya, A. Singh, J. Meitzner, D. Aher, H. Yang, J. Romero, B. Chen, C. Hsu, K. C. Cheng, Y. Chang, M. Sarmiento, C. Grange, E. Mazaleyrat and K. Rochereau, in *2021 IEEE International Electron Devices Meeting (IEDM)*, 2021, p. 23.4.1-23.4.4.

10 G. Konstantatos, I. Howard, A. Fischer, S. Hoogland, J. Clifford, E. Klem, L. Levina and E. H. Sargent, *Nature*, 2006, **442**, 180–183.

11 A. S. Shikoh, G. S. Choi, S. Hong, K. S. Jeong and J. Kim, *Nanotechnology*, 2022, **33**, 165501.

12 C. Gréboval, A. Chu, N. Goubet, C. Livache, S. Ithurria and E. Lhuillier, *Chem. Rev.*, 2021, **121**, 3627–3700.

13 Z. Deng, K. S. Jeong and P. Guyot-Sionnest, *ACS Nano*, 2014, **8**, 11707–11714.

14 S. B. Hafiz, M. M. Al Mahfuz, M. R. Scimeca, S. Lee, S. J. Oh, A. Sahu and D.-K. Ko, *Phys. E Low-Dimens. Syst. Nanostructures*, 2020, **124**, 114223.

15 M. Park, D. Choi, Y. Choi, H. Shin and K. S. Jeong, *ACS Photonics*, 2018, **5**, 1907–1911.

16 J. Qu, N. Goubet, C. Livache, B. Martinez, D. Amelot, C. Gréboval, A. Chu, J. Ramade, H. Cruguel, S. Ithurria, M. G. Silly and E. Lhuillier, *J. Phys. Chem. C*, 2018, **122**, 18161–18167.

17 A. Rogach, S. V. Kershaw, M. Burt, M. T. Harrison, A. Kornowski, A. Eychmüller and H. Weller, *Adv. Mater.*, 1999, **11**, 552–555.

18 M. V. Kovalenko, E. Kaufmann, D. Pachinger, J. Roither, M. Huber, J. Stangl, G. Hesser, F. Schäffler and W. Heiss, *J. Am. Chem. Soc.*, 2006, **128**, 3516–3517.

19 C. Gréboval, D. Darson, V. Parahyba, R. Alchaar, C. Abadie, V. Noguier, S. Ferré, E. Izquierdo, A. Khalili, Y. Prado, P. Potet and E. Lhuillier, *Nanoscale*, 2022, **14**, 9359–9368.

20 Y. Dong, M. Chen, W. K. Yiu, Q. Zhu, G. Zhou, S. V. Kershaw, N. Ke, C. P. Wong, A. L. Rogach and N. Zhao, *Adv. Sci.*, 2020, **7**, 2000068.

21 M. Chen, H. Lu, N. M. Abdelazim, Y. Zhu, Z. Wang, W. Ren, S. V. Kershaw, A. L. Rogach and N. Zhao, *ACS Nano*, 2017, **11**, 5614–5622.

22 U. N. Noumbé, C. Gréboval, C. Livache, A. Chu, H. Majjad, L. E. Parra López, L. D. N. Mouafo, B. Doudin, S. Berciaud, J. Chaste, A. Ouerghi, E. Lhuillier and J.-F. Dayen, *ACS Nano*, 2020, **14**, 4567–4576.

23 M. Chen, L. Lu, H. Yu, C. Li and N. Zhao, *Adv. Sci.*, 2021, **8**, 2101560.

24 M. M. Ackerman, X. Tang and P. Guyot-Sionnest, *ACS Nano*, 2018, **12**, 7264–7271.

25 J. Yang, Y. Lv, Z. He, B. Wang, S. Chen, F. Xiao, H. Hu, M. Yu, H. Liu, X. Lan, H.-Y. Hsu, H. Song and J. Tang, *ACS Photonics*, , DOI:10.1021/acsphotonics.2c01145.

26 P. Rastogi, E. Izquierdo, C. Gréboval, M. Cavallo, A. Chu, T. H. Dang, A. Khalili, C. Abadie, R. Alchaar, S. Pierini, H. Cruguel, N. Witkowski, J. K. Utterback, T. Brule, X. Z. Xu, P. Hollander, A. Ouerghi, B. Gallas, M. G. Silly and E. Lhuillier, *J. Phys. Chem. C*, 2022, **126**, 13720–13728.

27 C. Gréboval, E. Izquierdo, C. Abadie, A. Khalili, M. Cavallo, A. Chu, T. H. Dang, H. Zhang, X. Lafosse, M. Rosticher, X. Z. Xu, A. Descamps-Mandine, A. Ouerghi, M. G. Silly, S. Ithurria and E. Lhuillier, *ACS Appl. Nano Mater.*, 2022, **5**, 8602–8611.

28 M. Chen and P. Guyot-Sionnest, *ACS Nano*, 2017, **11**, 4165–4173.

29 A. Jagtap, B. Martinez, N. Goubet, A. Chu, C. Livache, C. Gréboval, J. Ramade, D. Amelot, P. Trousset, A. Triboulin, S. Ithurria, M. G. Silly, B. Dubertret and E. Lhuillier, *ACS Photonics*, 2018, **5**, 4569–4576.

30 A. Chu, B. Martinez, S. Ferré, V. Noguier, C. Gréboval, C. Livache, J. Qu, Y. Prado, N. Casaretto, N. Goubet, H. Cruguel, L. Dudy, M. G. Silly, G. Vincent and E. Lhuillier, *ACS Appl. Mater. Interfaces*, 2019, **11**, 33116–33123.

31 M. Cavallo, E. Bossavit, H. Zhang, C. Dabard, T. H. Dang, A. Khalili, C. Abadie, R. Alchaar, D. Mastrippolito, Y. Prado, L. Becerra, M. Rosticher, M. G. Silly, J. K. Utterback, S. Ithurria, J. Avila, D. Pierucci and E. Lhuillier, *Nano Lett.*, , DOI:10.1021/acs.nanolett.2c04637.

32 F. Joucken, J. Avila, Z. Ge, E. A. Quezada-Lopez, H. Yi, R. Le Goff, E. Baudin, J. L. Davenport, K. Watanabe and T. Taniguchi, *Nano Lett.*, 2019, **19**, 2682–2687.

33 J. Avila and M. C. Asensio, *Synchrotron Radiat. News*, 2014, **27**, 24–30.

34 C. J. Blomfield, *J. Electron Spectrosc. Relat. Phenom.*, 2005, **143**, 241–249.

35 O. Renault, H. Kim, D. Dumcenco, D. Unuchek, N. Chevalier, M. Gay, A. Kis and N. Fairley, *J. Vac. Sci. Technol. A*, 2021, **39**, 053210.

36 M. Cattelan and N. A. Fox, *Nanomaterials*, 2018, **8**, 284.
37 J. Ye, Y. Li, A. A. Medjahed, S. Pouget, D. Aldakov, Y. Liu and P. Reiss, *Small*, 2021, **17**, 2170020.
38 J. Avila, I. Razado-Colambo, S. Lorcy, B. Lagarde, J.-L. Giorgetta, F. Polack and M. C. Asensio, *J. Phys. Conf. Ser.*, 2013, **425**, 192023.
39 F. Polack, M. Silly, C. Chauvet, B. Lagarde, N. Bergeard, M. Izquierdo, O. Chubar, D. Krizmancic, M. Ribbens, J. -P. Duval, C. Basset, S. Kubsky and F. Sirotti, *AIP Conf. Proc.*, 2010, **1234**, 185–188.
40 S. Keuleyan, E. Lhuillier and P. Guyot-Sionnest, *J. Am. Chem. Soc.*, 2011, **133**, 16422–16424.
41 B. Martinez, J. Ramade, C. Livache, N. Goubet, A. Chu, C. Gréboval, J. Qu, W. L. Watkins, L. Becerra, E. Dandeu, J. L. Fave, C. Méthivier, E. Lacaze and E. Lhuillier, *Adv. Opt. Mater.*, 2019, **7**, 1900348.
42 X. Lan, M. Chen, M. H. Hudson, V. Kamysbayev, Y. Wang, P. Guyot-Sionnest and D. V. Talapin, *Nat. Mater.*, 2020, **19**, 323–329.
43 H. Zhang, R. Alchaar, Y. Prado, A. Khalili, C. Gréboval, M. Cavallo, E. Bossavit, C. Dabard, T. H. Dang, C. Abadie, C. Methivier, D. Darson, V. Parahyba, P. Potet, J. Ramade, M. G. Silly, J. K. Utterback, D. Pierucci, S. Ithurria and E. Lhuillier, *Chem. Mater.*, 2022, **34**, 10964–10972.
44 X. Xue, M. Chen, Y. Luo, T. Qin, X. Tang and Q. Hao, *Light Sci. Appl.*, 2023, **12**, 2.
45 N. Moghaddam, C. Gréboval, J. Qu, A. Chu, P. Rastogi, C. Livache, A. Khalili, X. Z. Xu, B. Baptiste, S. Klotz, G. Fishman, F. Capitani, S. Ithurria, S. Sauvage and E. Lhuillier, *J. Phys. Chem. C*, 2020, **124**, 23460–23468.
46 H. Jo, J. K. Kim, J. Kim, T.-Y. Seong, H. J. Son, J.-H. Jeong and H. Yu, *ACS Appl. Energy Mater.*, 2021, **4**, 13776–13784.